

Gibbs states and Brownian models for coexisting haze and cloud droplets

Manuel Santos-Gutiérrez, Mickaël D. Chekroun,* and Ilan Koren

Department of Earth and Planetary Sciences, Weizmann Institute of Science, Rehovot 76100, Israel

(Dated: March 10, 2024)

Clouds microphysics describes the formation and evolution of cloud droplets, rain, and ice particles. It is among the most critical factors in determining the cloud's size, lifetime, precipitation, and radiative effect. Among all cloud types, the small clouds, characterized by weak updrafts, that are close to the haze-to-cloud transition pose challenges in measuring them and understanding their properties. They are superabundant but hard to capture by satellites and often falsely regarded as aerosols. Köhler's theory explains droplet activation and their growth by condensation at the earliest stages of cloud development. It fully describes the thermodynamic state of a single drop but falls short when explaining the collective behavior of large populations of particles. This is especially important when the supersaturation pool is limited. We present an analytical framework to extend Köhler's theory to coexisting cloud droplets. Our results suggest hysteresis and asymmetry in the process of droplet activation and deactivation. The turbulent nature of clouds is incorporated into our model formulation as Brownian noise to provide explicit droplet size distributions and activation timescales. The theoretical findings are confronted with experimental data stemming from laboratory clouds created in the Pi convection chamber, suggesting a new way of understanding haze-to-cloud transitions and small cloud formation processes.

INTRODUCTION

Clouds play a key role in the climate energy balances and in the water cycle [1]. A large part of the uncertainties in climate predictions is attributed to limitations in our understanding of cloud physics and therefore, how to parameterize such clouds in global climate models [2]. Out of all cloud types, a great part of the cloud research challenges is attributed to small, warm clouds that are highly abundant but hard to measure. Many of these clouds are too small relative to earth-observing satellites' resolution, and/or their optical signature is too weak [3–5].

The cloud's droplet size distribution (DSD) is among the most important microphysical properties. The DSD properties are coupled to all dynamical, turbulent, optical, and stochastic cloud processes. DSDs affect the cloud's evolution in time, rain processes, cloud depth, size, and lifetime [6]. When supersaturation is high enough, cloud condensation nuclei (CCNs) are activated into cloud droplets and grow by condensation. This is the main mechanism for droplet growth at the early stages of a warm cloud. If the cloud's dynamics is weak (shallow clouds) or if the aerosol concentration is high, growth droplets by condensation could be the main mechanism throughout the whole cloud's lifetime as droplets do not become large and varied enough to support efficient autoconversion of droplets by the stochastic processes of collision and coalescence [7, §7-8].

In warm clouds that are controlled by weak updrafts and low supersaturations, only a small part of the aerosol (the large and most hygroscopic) are activated. A competition between the droplet curvature (Kelvin) effect, which suppresses activation, and the solute (Raoult) effect, which reduces the critical supersaturation for activation, [8] allows for suspended particles in air parcels to coexist in two main thermodynamical states known as: *haze* and *activated droplet* [6]. While hazy particles are in stable equilibrium, activated particles harvest the available water vapor and grow until equilibrium is restored.

The mechanisms of activation and deactivation are, however, not symmetric. In order to activate a cloud droplet, it is necessary to attain a critical level of supersaturation λ_K , typically well above 0%. When supersaturation is decreased to λ_K in the deactivation process, an activated cloud droplet is big enough to still experience diffusion of water vapor onto its surface and, hence, it is expected that this positive feedback makes the threshold for deactivation strictly lower than that of λ_K . Consequently, activation-deactivation undergoes hysteresis, which has been previously reported in the cloud physics literature [9, 10]. From a theoretical perspective, in the work of [10] it was shown on analytical grounds that the activation process of a cloud particle undergoes a saddle-node bifurcation and, when coupled to supersaturation evolution, hysteresis is numerically observed in a parcel model and attributed to kinetic limitations and the presence of a cusp bifurcation [11, §8.2].

Another level of complexity in the determination of microphysical properties concerns clouds living in eminently turbulent environments. Indeed, turbulence heavily influences the life cycle of clouds; see [12] for a review on the topic. In particular, the incorporation of turbulent models provides the means to explain droplet size spectra broadening [13, 14], as well as describe the mixing of the cumulus clouds with their exterior [5, 15] and parameterize mixed-phase clouds in global circulation models [16, 17]. In the context of warm clouds, localized temperature gradients and turbulence at the smallest scales provoke supersaturation fluctuations that allow activation of haze particles even in mean-subsaturated environments [18], and similarly, cloud particles susceptible of deactivating [15]. Thus, microphysical fluctuations are a key feature in obtaining faithful descriptions of droplet size spectra.

This research explores the activation and deactivation of cloud droplets in warm clouds, offering new theoretical perspectives. We aim to find analytical formulas for describing the size distribution of droplets (DSDs) when both small cloud droplets and haze particles coexist, assuming condensation as the only growth mechanism. Similar to previous work [10], we analyze how droplet growth due to condensation changes dramatically as the surrounding air's supersaturation level varies.

*Electronic address: michael-david.chekroun@weizmann.ac.il

To the Köhler instability we add a sink term in growth rate which aims at (i) modeling the supersaturation budget, and (ii) parameterising other stagnating mechanisms into the condensational growth, for instance, due to sedimentation [19] or the presence of a thermal inversion layer that reduces supersaturation and stops droplet growth [20, 21]. The resulting equation describing condensation growth for droplets of a uniform size allows for multiple stable states to co-exist besides the “haze” state, meaning the system exhibits multistability. Although the haze state remains stable, this multistability suggests that activated droplets can get stuck around a specific size due to the balancing act between two factors: the Köhler instability and mechanisms that decrease supersaturation or remove particles; see also [9, 10, 22].

However, turbulence effects throw a wrench in the picture. The stable states become “fuzzy states” that are encountered statistically (metastable) at various rates of occurrence. This means that particles can switch between activated and deactivated states, similar to how Brownian particles move around in a bumpy landscape. These turbulent jolts also significantly impact the activation-deactivation process into the form of various possible hysteresis loops (see Fig. 5 below). As a result, droplets can become activated at lower levels of supersaturation compared to the standard Köhler threshold.

Finally, our framework allows us to derive analytical formulas for the size distribution of droplets (DSDs) within a cloud volume, accounting for these stochastic turbulent effects. In particular, our stochastic model predicts that droplet size distributions in Pi cloud convection chamber experiments behave like Gibbs states. It is shown that this prediction closely matches the actual DSDs observed in these experiments (see Fig. 6 below).

RESULTS

Köhler theory

The theory of Köhler is the thermodynamical backbone to explain the formation of cloud droplets out of suspended aerosols in the atmosphere. It establishes the critical relative humidity threshold beyond which suspended particles activate and grow by diffusion (condensation) [8]. The critical threshold is above saturation (hence, the supersaturation term is used), and it depends on the initial size and chemical composition of the particle in question. These particles are, according to Köhler, present in two distinct/dichotomical thermodynamic states: The first is known as *haze* and it is observed when the aerosol is humidified, although remains at equilibrium with its moist environment. The second state is referred to as *activated droplet*, whereby the particle harvests the available moisture by diffusion and, in principle, grows indefinitely. However, in nature, the available water molecules that are in supersaturation are limited, and in many cases, droplets and haze coexist in the cloud, and particles can oscillate between the two states. Particularly, in cases of small, warm clouds [21, 23].

The critical relative humidity threshold needed for activation of a given aerosol with a solubility constant k and a dry radius r_d is analytically obtained using the Köhler’s equation [7, 8]. Here, to simplify some derivations, λ denotes the part of the relative humidity above 100%. If $r(t)$ denotes the radius of a

TABLE I: Köhler curve’s parameters for NaCl.

	k	r_d (μm)	A (μm)	D ($\mu\text{m}^2\text{s}^{-1}$)
NaCl	1.28	5×10^{-2}	10^{-3}	40

given droplet at time t , its evolution is approximated by [8, 10]:

$$\begin{cases} \dot{r} = \frac{D}{r}(\lambda - \lambda_{eq}(r)) \\ \lambda_{eq}(r) = \frac{A}{r} - \frac{B}{r^3}, \end{cases} \quad (1)$$

where D is the diffusivity constant, A relates to the water surface tension, $B = kr_d^3$, λ is the ambient supersaturation and $\lambda_{eq}(r)$ determines the equilibrium supersaturation at the surface of a droplet of radius r ; commonly known as *Köhler curve* [24]. Equation (1) shows that the particle is in equilibrium when $\lambda = \lambda_{eq}(r)$. To simplify the proposed model, we replace r with the variable $X = r^2/2D$, which has time-units and could be viewed as relaxation time for diffusion. With this change of variable, Eq. (1) translates into the nondimensional form:

$$\begin{cases} \dot{X} = \lambda - f(X), \\ f(X) = A(2DX)^{-1/2} - B(2DX)^{-3/2}, \end{cases} \quad (2)$$

with $f(X)$ denoting the equilibrium supersaturation $\lambda_{eq}(r)$ as function of X . A rudimentary analysis of $f(X)$ reveals a single global maximum located at $X_K = 3B/(2DA)$, and with critical supersaturation value $\lambda_K = f(X_K) = (4A^3/27B)^{1/2}$, see also [24, §6.1]. An example of Köhler curve is shown in Fig. 1a) whose parameters are given in Table I. This curve reaches its maximum at $X_K = 6 \cdot 10^{-3}\text{s}$, or at $r^2 = 0.48\mu\text{m}^2$.

For a given dry radius r_d , when the supersaturation λ exceeds the corresponding λ_K , the particle is activated into a cloud droplet and grows by diffusion. On the contrary, for a given ambient supersaturation λ , particles whose radii are less than $(2DX_u)^{1/2}$ remain stable in a haze state; see Fig. 1a).

While Köhler theory is established for single particles, clouds consist of large families of particles coexisting in the same humidity environment. When a collection of droplets consumes the available supersaturation, the particles may cease growing by condensation, and the droplet size distributions (DSDs) stagnate and stop being displaced towards larger sizes. Here we modify the Köhler equation to the case of many particles in conditions of small warm clouds, when the available supersaturation is a limit factor. The proposed model extends the condensational growth equation—governed by the Köhler curve—by coupling all particles to supersaturation consumption and by adding stochastic disturbances, to account for (micro) small-scale turbulent effects.

Multistable Köhler curves

In cases with relatively small supersaturation, as particles grow, they may consume the available supersaturation and therefore reduce their growth rate until reaching stagnation. In the realm of single-particle models these effects can be

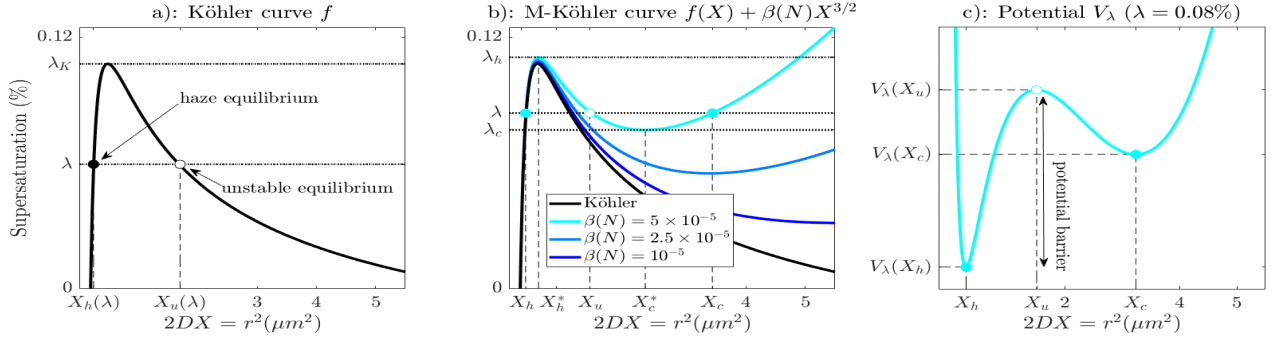


FIG. 1: **Panel a)**: Köhler curve associated with NaCl; see Table I for the parameter values. A dry radius of 50nm is prescribed. λ_K denotes Köhler's critical supersaturation and λ , an example of supersaturation. **Panel b)**: In black, the Köhler curve associated with NaCl as Panel a). The cyan to blue curves show different M-Köhler curves associated with Eq. (6) for different values of the parameter $\beta(N)$ as indicated in the legend. For the cyan curve are shown furthermore its intersection with a given supersaturation λ in between λ_c and λ_h . Each filled dot corresponds to a stable equilibrium while the empty dot corresponds to the unstable equilibrium. **Panel c)**: The potential function associated with the cyan M-Köhler curve for the supersaturation value as indicated in the title. The solid/empty dots locate the stable/unstable equilibria.

modeled by the introduction of a *sink* function into Eq. (1):

$$\dot{X} = \lambda - \underbrace{(f(X) - g(X))}_{\text{M-Köhler curve}}, \quad (3)$$

in which g denotes the sink term. The function $f - g$ is called a *M-Köhler curve* hereafter. The term g should remain negative and should decrease as X increases. The sink term in growth rate aims at (i) modeling the supersaturation budget, and (ii) parameterizing other stagnating mechanisms into the condensational growth, for instance, due to sedimentation [19] or the presence of a thermal inversion layer that reduces supersaturation and stops droplet growth [20, 21].

The sink term can also relate to first-order fluctuations in supersaturation. Indeed, when a sizable amount of particles coexist in the same cloud parcel, the constant supersaturation assumption has to be amended taking account changes in λ in the course of time, assuming λ in Eq. (3) to be time-dependent. At a first order, we are concerned with describing the evolution of $\lambda(t) = \lambda + \lambda'(t)$ with $\lambda'(0) = 0$, i.e. we are seeking for a model of the rate of change of the fluctuations λ' around a given value λ .

Following [10], the rate of change λ' can be approximated by the ratio $-\dot{\rho}_v/\rho_{vs}$, in which ρ_v denotes the ambient vapour density away from the droplet while, ρ_{vs} , denotes the vapour density at saturation. Then, by expressing ρ_v as $\rho_v = 4\pi N \rho_w r^3/3$, accounting for the density of liquid water ρ_w and the droplet volume concentration N of identical (monodisperse) particles in the cloud parcel, we arrive at:

$$\dot{\lambda}' = -\beta(N) \left(\dot{X}^{\frac{3}{2}} \right), \quad (4)$$

when written in the variable $X = r^2/(2D)$, where the constant $\beta(N)$ is given by

$$\beta(N) = \frac{2^{7/2} D^{3/2} \pi \rho_w}{3 \rho_{vs}} N; \quad (5)$$

see [10, Eqns. (9) and (10)].

The integration of Eq. (4) yields to $\lambda(t) = \lambda - \beta(N)X^{3/2}$ which eventually leads to the following condensational growth

model:

$$\dot{X} = \lambda - f(X) - \beta(N)X^{3/2}. \quad (6)$$

Thus, the term $-\beta(N)X^{3/2}$ acts as the sink function g in Eq. (3): it is negative and decreases as X increases. For large values of X , it saturates the particle growth. A few M-Köhler curves are shown in Fig. 1b), for different $\beta(N)$ -values.

A careful examination of Eq. (6) reveals that Köhler's critical supersaturation λ_K and radius are modified due to the sink function. In fact, the function $f(X) + \beta(N)X^{3/2}$ can now admit a local minimum additional to the maximum exhibited by the Köhler curve f . These are obtained as zeros of the following depressed cubic polynomial equation:

$$-3\beta(N)X^3 + A(2D)^{-1/2}X - 3B(2D)^{-3/2} = 0. \quad (7)$$

Sufficient conditions for Eq. (7) to have two positive solutions are easily derivable. Actually, a simple proposition inferring the existence of two positive steady states X_h^* and X_c^* (with $X_c^* \geq X_h^*$) to condensational growth model analogues to Eq. (6) for a sink function $-\beta(N)X^\alpha$ ($\alpha > 1$) is derived in in *Methods* (see Proposition 1 therein). In any event, as shown in Fig. 1b) the locations of X_h^* and X_c^* depend on the strength of the sink function's coefficient $\beta(N)$.

We define then the following supersaturation values $\lambda_h = f(X_h^*) - g(X_h^*)$, which corresponds to the local maximum of $f - g$, and $\lambda_c = f(X_c^*) - g(X_c^*)$, corresponding to its local minimum. In particular, $\lambda_h \geq \lambda_c$.

Due to the presence of this new local minimum (compared to the Köhler curve), as supersaturation λ varies, the number of equilibria varies through two saddle-node bifurcations, as summarized in Fig. 2. These two saddle-node bifurcations provide the nonlinear backbone for hysteresis to take place as discussed in *Hysteresis effects*, below. These hysteresis effects are well-known to be revealed in presence of stochastic disturbances; see e.g. [25]. We discuss below the physical motivation of introducing such disturbances in Eq. (6) or more generally, Eq. (3).

Brownian models and turbulent effects

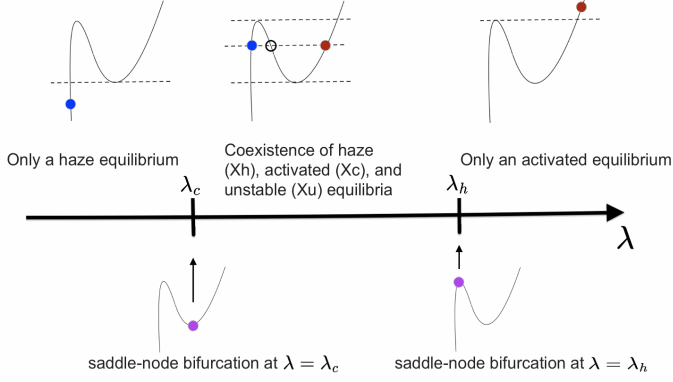


FIG. 2: **Going through multiple equilibria as λ varies.** Two saddle-node (SN) bifurcations occur, one at $\lambda = \lambda_c$ and one at $\lambda = \lambda_h$. For $\lambda < \lambda_c$, there is only a hazy stable equilibrium X_h (blue dot in the leftmost upper diagram). As one crosses from below the SN bifurcation point at $\lambda = \lambda_c$, two other equilibria emerge for a total of 3 equilibria coexisting for $\lambda_c < \lambda < \lambda_h$ (middle upper diagram): an *activated* stable equilibrium X_c (red dot), an unstable equilibrium X_u (open circle), and a hazy equilibrium (blue dot). At the SN bifurcation occurring at $\lambda = \lambda_h$, X_u and X_h collide (purple dot on the rightmost lower diagram), and only the activated equilibrium survives as $\lambda > \lambda_h$ (red dot in the rightmost upper diagram).

In a developing cloud, turbulent updrafts and mixing with its neighboring air provoke supersaturation fluctuations that naturally affect droplet growth and, consequently, the collective droplet size spectra [14, 15]. Stochastic models for the velocity fluctuations and the supersaturation fields have been considered in previous studies and have shown various degrees of relevance [13, 26]. For a cloud parcel subject to turbulent updrafts, the authors in [13] prove that activated droplet size variance increases, at short times, proportionally to the square-root of time, analogous to Einstein’s diffusion formula. Their analytical findings are contrasted with direct numerical simulations of turbulence obeying the incompressible Navier-Stokes equation. In spite of this diffusion result with diverging variance, in [26], the authors find a statistical steady state for droplet size, with DSDs characterized by exponential tails; see their Eq. (4.3). Noteworthy is that to achieve convergence to a steady state, a substantial proportion of the droplets must reach evaporation, possibly if, on average, they experience negative supersaturations.

Supersaturation being the driving parameter, we assume that it evolves around a given value λ with fluctuations encoded by a stochastic term possibly depending on the particle size. For the sake of generality, we aim at modeling the inhomogeneous effects of supersaturation fluctuations on droplets of different size. Indeed, this size-dependent fluctuations appear, for instance, when taking the adiabatic limit of fast supersaturation fluctuations, as demonstrated in [26, Eq. (4.3)]. Hence, incorporating different supersaturation sources and sinks alter the expression for the noise law affecting droplet growth. Such noise inhomogeneity is here motivated from the fact that small fluctuations in droplet radius incur greater fluctuations in supersaturation when the particles are bigger. Contrary to hazy particles, which are at a stable thermodynamic equilibrium and variations in their radius provoke smaller alterations in the supersaturation budget.

These considerations invite us to parameterize the fluctu-

ations of λ by means of a size-dependent stochastic term, $\sigma(X)\dot{W}_t$, leading to the following stochastic model:

$$\dot{X} = \underbrace{\lambda - f(X) + g(X)}_{-V'_\lambda(X)} + \sigma(X)\dot{W}_t, \quad (8)$$

where W_t is a Brownian motion (and \dot{W}_t is Gaussian and white).

The function V_λ is the potential function that collects the nonlinear, deterministic effects in the model. Thus, the solutions $X(t)$ to Eq. (8) can be regarded as Brownian particles embedded in the potential V_λ defined in Eq. (8). The equilibria of Eq. (3) correspond exactly to the local critical points of the potential function—see Fig. 1c—and their stability is determined by the local curvature of V_λ at those points, see e.g. [25, 27]. Note that Eq. (8) can always be recast into a form in which the stochastic disturbance term becomes X -independent, at the expense of changing the potential function via the Lamperti transformation [27, §3.6]. This trick is recalled in *Methods* as it is also part of our model’s analysis below.

For a family of monodisperse droplets in the same cloud volume, each one experiences different supersaturation fluctuations, albeit with the same mean and variance, as encapsulated by the term $\sigma(X)\dot{W}_t$ in Eq. (8). When each supersaturation’s stochastic realization is averaged over a large number of particles, the Fokker-Planck Equation (FPE) associated with Eq. (8) provides the DSD at a given time t ; see e.g. [27, 28]. The stationary solution to the FPE is then given analytically and known as the *Gibbs state* [27, Eq. (4.35)]:

$$\rho_\lambda(X) = Z_\lambda^{-1} \frac{\exp\left(2 \int^X \frac{\lambda - f(x) + g(x)}{\sigma^2(x)} dx\right)}{\sigma^2(X)}, \quad (9)$$

where Z_λ is a normalizing constant. This distribution is a generalization of what is found in [29, Eq. (6)]. Such equation yields a Weibull distribution for droplet radius r , without considering curvature and chemistry effects, i.e. Köhler theory, sink functions or state-dependent noise. One can, thus, derive the Weibull distribution ρ_W for the radius r by setting $f = g \equiv 0$ and σ constant, where the resulting DSD is integrable only if there is mean subsaturation, $\lambda < 0$:

$$\rho_W(r) = Z_\lambda^{-1} r e^{\gamma r^2}, \quad (10)$$

where γ is a parameter proportional to λ , droplet number concentration and liquid water fraction; see [29, Eq. (8)]. In comparison, ρ_λ in Eq. (9) can be integrable if λ is positive, provided that the sink function g has suitable decay properties detailed in Proposition 2 found in *The confining potential* in *Methods*. For instance considering sedimentation, or any size-independent removal mechanism, would provide an integrable DSD; see [19] and [22, Sections 2.1, 2.2 and 2.3], where the resulting DSDs are an explicit evaluation of ρ_λ in Eq. (9).

For a broad class of f , g and σ , the Gibbs state ρ_λ exhibits multimodality intimately related to shape of the potential V_λ . More precisely, the Gibbs state’s modes, the local maxima of ρ_λ , are found by solving the following equation:

$$-V'_\lambda(X) = \frac{1}{2} \sigma'(X) \sigma(X). \quad (11)$$

See *Noise-induced metastability* in *Methods* for the derivation of this equation. This fundamental equation teaches us how the Gibbs state modes result from the interaction between the noise term and the potential function. The Gibbs state's modes correspond to metastable states for which the random fluctuation term, $\sigma(X)\dot{W}_t$, in Eq. (8) acts as a source for the particles to experience transitions from a statistically typical droplet size to another one; see schematic of Fig. 3.

When the noise is state-independent, i.e. when $\sigma(X) = \sqrt{2\varepsilon}$, then $\sigma'(X) = 0$ and the metastable states are directly determined by the zeros of $-V'_\lambda$. In this case, for Eq. (6), the Gibbs states are *bimodal* when $\lambda_c < \lambda < \lambda_h$, and *unimodal* when there is just one underlying stable equilibrium, i.e. for either $\lambda < \lambda_c$ or $\lambda > \lambda_h$; see Fig. 2. When $\lambda_c < \lambda < \lambda_h$, there is a non-vanishing probability of encountering haze or activated droplets; see Fig. 3. This property is consistent with realistic situations in which turbulent supersaturation fluctuations make haze susceptible of activating even if *on average* the Köhler's threshold is not attained [18].

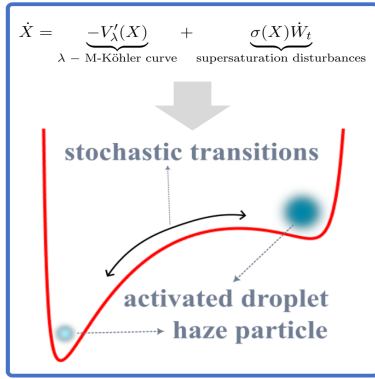


FIG. 3: **Cartoon of haze-to-droplet stochastic transitions.** Here λ is kept fixed and the situation depicted corresponds to λ in (λ_c, λ_h) where coexist two stable states (haze particle and activated droplet); see Fig. 2.

Our modeling allows for other useful analytic insights. For instance, the expected residence times at the haze or activated state can be precisely determined. They are indeed known to relate to the potential barrier, $V_\lambda(X_u) - V_\lambda(X_h)$ (see Fig. 1c), according to the Kramers' time formulas [25, 30]. The mean activation time τ_{act} is then given by [31, Eq. (2.19)]

$$\tau_{act}(\lambda) = \frac{2\pi}{\sqrt{|V''_\lambda(X_u)|V''_\lambda(X_h)}} e^{\frac{V_\lambda(X_u) - V_\lambda(X_h)}{\varepsilon}}. \quad (12)$$

Therefore, the closer λ is to the critical value λ_h from below, the closer X_u is to a collision with X_h (see Fig. 2) and the shallower the potential barrier becomes, resulting into more common particle activation. Similarly, deactivation of activated droplets can take place due to fluctuations in supersaturation with a mean deactivation time obtained by (12) in which X_h is replaced by X_c .

Hysteresis effects

The hysteresis behavior pointed out at the end of *Multistable Köhler curves* is now analyzed when the supersaturation parameter λ is allowed to drift through the critical values λ_c and λ_h , slower compared to the stochastic fluctuations. Such relatively slower variations in λ are associated with buoyancy-driven supersaturation changes. Supersaturation λ increases

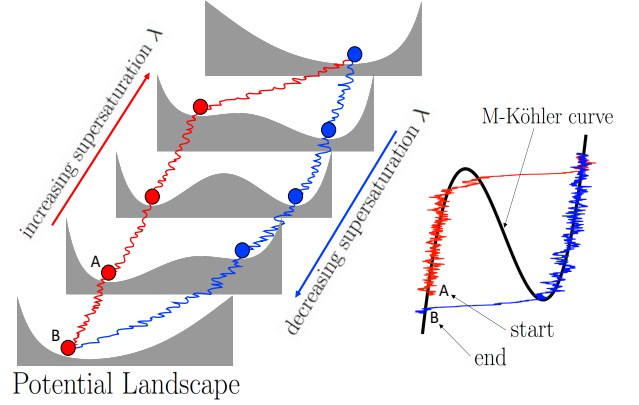


FIG. 4: **Rationale of an hysteresis path.** As λ varies, the potential landscape changes and the stochastic disturbances can help trigger the critical transition as one approaches the tipping points, here the saddle-node bifurcation points.

as the buoyant parcel rises until the activation threshold λ_h is attained and some of the contained haze is activated. When the parcel ceases to be buoyant or reaches a temperature inversion, supersaturation decreases to λ_c , below which the whole family of droplets regenerates into haze. During this buoyancy-cycle, the population of particles faces a continuous change in the potential V_λ , as illustrated in Fig. 4, for increasing and decreasing supersaturation levels. It is there shown the asymmetry of activation. Indeed, when a haze particle undergoes activation—starting at point A and following the red, wobbly line—, its deactivation will occur at much lower supersaturation levels—as seen when following the blue wobbly line that ends in point B—. Similar cycles have also been reported in the absence of aerosol curvature and chemistry effects, and uniquely due to noisy supersaturation fluctuations around a subsaturated mean; see [26, Fig. 4].

Within the present framework, it remains to investigate the effects of (i) different rates of changes in supersaturation and (ii) variations in the magnitude of the fast supersaturation fluctuations as encapsulated by the noise term. The hysteresis phenomenon under the presence of noise has been investigated in previous work [32], where it is found that a large (additive) noise variance σ , on average, reduces the area of hysteresis loops. In our context, this implies that droplet activation can occur at much lower supersaturation values compared to λ_h . To numerically examine these ideas, we solve the Eq. (8) associated with the sink term $g(X) = -\beta(N)X^{3/2}$ used in Eq. (6), for specific noise variances and mean supersaturation λ ranging from 0.06% to 0.11% with different linear rate $\dot{\lambda}$.

The numerical experiments regarding hysteresis are shown in Fig. 5, where Eq. (6) was integrated using an Euler-Maruyama scheme with a time step of 10^{-2} s. In Fig. 5a), b) and c), are shown hysteresis paths solving Eq. (6) for three rates of change $\dot{\lambda}$. As expected, when the rate of change in supersaturation is not slow enough, it can prevent droplet activation—see Fig. 5a)—, whereas sufficiently slow, adiabatic changes enforce the droplet size to follow the M-Köhler curve such as shown in Fig. 5c). As a haze particle experiences an increase in supersaturation—resulting from an adiabatic cooling of a cloud parcel—this will grow by condensation following the

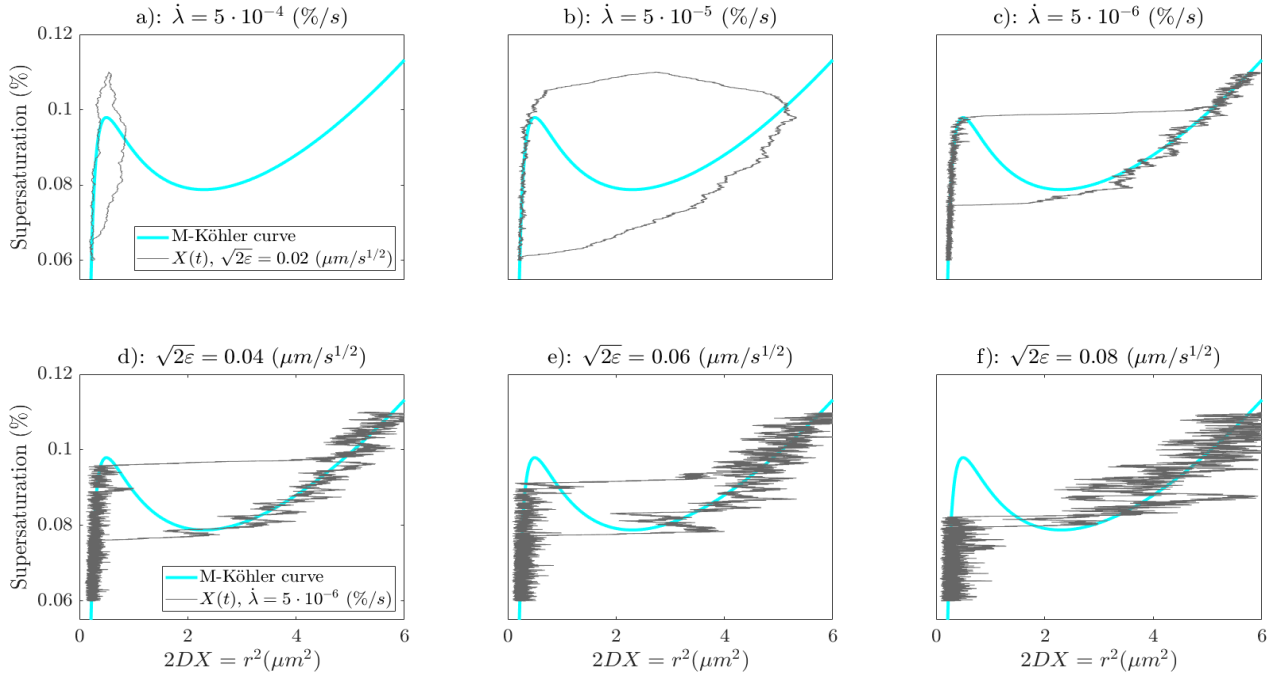


FIG. 5: **Panels a), b) and c):** The thin gray line indicates the hysteresis loops for different rates of change of supersaturation $\dot{\lambda}$ as indicated in the title. The noise variance is constant for these three panels as indicated in the legend of Panel a). **Panels d), e) and f):** The thin gray lines indicate the hysteresis loops for different noise variances as indicated in the titles. The rate of change of supersaturation $\dot{\lambda}$ is constant for these three panels as indicated in the legend of Panel d). For all panels, the cyan line is the M-Köhler curve associated with Eq. (6) and $\beta(N) = 3.6 \times 10^{-2} s^{-3/2}$.

Köhler curve, almost regardless of how intense the cooling rate is, here indicated by $\dot{\lambda}$. This is an indication of the stability of the thermodynamic equilibrium of haze particles as opposed to cloud droplets, which are more sensitive to the cooling rate $\dot{\lambda}$. Indeed, by comparing Figs. 5b) and c), we observe that only when the cooling rate is slowest do we observe a droplet growth attached to the Köhler curve.

Panels d), e) and f) of Figure 5 provide an illustration of results of [32] for Eq. (6). Here we show the effects of increasing turbulent noise intensity as a haze particle grows and activates in a slowly cooling air volume. In such case we are in the situation of Fig. 5c) where the particle's size is dictated by the Köhler curve— modulo zero-mean fluctuations—. As noise variance is increased, the hysteresis loop is collapsed to the extent that droplet activation is expected as soon as λ surpasses λ_c . Consequently, it is expected that slowly lifted humid parcels undergoing heaving turbulent updrafts— here encoded in the noise variance— can contain particles that activate at much lower supersaturations compared to that predicted by Köhler.

PI-Chamber Empirical Distributions vs Gibbs States

Small, warm convective clouds are abundant in the atmosphere but hard to measure [33]. Such clouds are often characterized by weak updrafts and small supersaturation, allowing for a significant part of the aerosol to coexist as haze together with the activated part [21, 23]. Cloud chambers are often used to study clouds in such thermodynamic conditions experimentally [18, 34].

In such work, the so-called Pi-chamber is seeded with monodisperse families of particles, and turbulent fluctuations are induced by changes in temperature, pressure, and aerosol

injection rates. Disregarding transients, the system reaches a steady state in number concentration and size distributions are calculated spanning hazy and active particles. Depending on the supersaturation mean and variance, DSDs display different characteristics involving their multimodality and spread; see [18, Fig. 2]. We show here that such experimental distributions are well approximated by the Gibbs states of our Brownian modelling framework once the sink and noise terms are appropriately designed. Our goal is to provide a qualitative and quantitative correspondence between the present theory and the experiments from [18].

We first address the sink term design. Note that for a monodisperse family of particles embedded in a cloud parcel, the supersaturation budget must be included in the collective droplet growth [9, 35]. Because the Pi-chamber is closed and in steady-state, the sink term affecting supersaturation is determined by water vapor condensation onto the particles. The mean sources of supersaturation are taken to be zero, apart from fluctuations encoded in $\sigma(X)$; see Eq. (8). Consequently, and to a first approximation, the initially prescribed supersaturation λ is consumed proportionally to the radius of the droplets, so that it evolves according to:

$$\lambda(t) \approx \lambda - \beta X(t)^{1/2} + \sigma(X)\dot{W}_t, \quad (13)$$

where the absorption parameter β depends on the number of active droplets, and the effective diffusivity of water vapour in air [6]. By substituting λ in the (standard) Köhler equation (1), the new term $-\beta X(t)^{1/2}$ plays the role of a sink term in Eq. (3), so that $g(X) = -\beta X^{1/2}$.

Regarding the term $\sigma(X)\dot{W}_t$, the inhomogeneous effect of fluctuations in haze and cloud droplets becomes apparent by

qualitatively examining the DSDs obtained in the Pi-chamber; see [18, Fig. 2]. To account for such dependence on particle size, we propose the following stochastic parameterization:

$$\begin{aligned}\sigma(X) &= \left(\sigma_1 + \frac{\sigma_2 - \sigma_1}{2} (1 + \psi(X)) \right), \\ \psi(X) &= \tanh(2\kappa D(X - X^*)).\end{aligned}\quad (14)$$

Here, the hyperbolic tangent is employed as a step function that allows for interpolating smoothly between the noise strengths that affect haze and activated particles, σ_1 and σ_2 respectively. Thus, we require that $\sigma_2 > \sigma_1 > 0$ for the reason stated above. The value of the slope is chosen to be sufficiently large—i.e., $2D\kappa = 10$ —so that the hyperbolic tangent approximates a step function, while still exhibiting the attributes of a smooth function, more amenable for analysis and numerical simulations. The “ignition” parameter X^* is chosen to be equal to $6.2 \cdot 10^{-3}$ s or, in diameter, $d^* = 1.41 \mu\text{m}$, which yields a correct location of the haze modes, and it is in the order of the critical Köhler diameter which is $d_K = 1.7 \mu\text{m}$. Such critical value is derived from Eq. (1), as explained in *Köhler theory*, for the curvature and solubility coefficients $A = 1.4 \cdot 10^{-3} \mu\text{m}$ and $B = 3.5 \cdot 10^{-4} \mu\text{m}^3$; see [18].

We, thus, arrive at the following Brownian model to describe cloud droplet size evolution in the Pi-chamber:

$$\dot{X} = \lambda - f(X) - \beta X^{1/2} + \sigma(X) \dot{W}_t, \quad (15)$$

with σ given by (14), and we recall that f is given by (2).

By solving Eq. (11) associated with Eq. (15), we can derive a relationship (valid for X sufficiently bigger than X^*) determining the parameter β in terms of the modal size X_c of the activated mode:

$$\beta = \frac{1}{X_c^2} \left(\lambda X_c^{3/2} - \frac{A}{(2D)^{1/2}} X_c + \frac{B}{(2D)^{3/2}} \right). \quad (16)$$

Eq. (16) plays a key role to estimate β : once β is known, the only parameters left for calibration of the model are σ_1 , σ_2 and the stiffness parameter κ .

We now confront the ability of our Brownian model (15) to approximate experimental DSDs by the Gibbs states formula (9). Three experimental setups are considered in that respect, following those of the Pi-chamber experiments from [18] corresponding to different supersaturation mean and fluctuation properties reported in such paper. These are referred to as according to [18]: a) *mean-dominated*, b) *fluctuation influenced* and c) *fluctuation dominated activation*.

Within our modeling framework, these regimes can be organized as follows:

Case I: $\lambda > \lambda_K \rightarrow$ mean-dominated activation

Case II: $\lambda_c < \lambda < \lambda_K \rightarrow$ fluctuation influenced activation

Case III: $\lambda < 1 \rightarrow$ fluctuation dominated activation

The parameter λ_K is the critical Köhler threshold, which is derived to be $\lambda \approx 1.00108$, for the type of aerosols considered in [18]. The steady-state supersaturation value in each case is also derived from [18]. Their theoretical calculations reveal indeed that Case I corresponds to $\lambda = 1\%$. While the value for

Case II is not explicitly provided, it can be inferred from our framework that λ is close to λ_h from below since a bimodal DSD is observed, with high peaks in the haze and activated domain: $\lambda = 0.1\%$ is taken for this case. Finally, Case III is a subsaturated regime ($\lambda < 0$) and as such we choose λ to be given by the Köhler’s value $f(X)$ at the haze peak’s location $X = X_h$, this gives $\lambda = -1\%$.

With these parameter values for λ , the parameter β can be estimated for Cases I and II according to Eq. (16), in which X_c is chosen to be the experimental DSD peak’s location that corresponds to activated droplets. For Case I, the modal activated diameter is $d_c = 18.109 \mu\text{m}$, giving $X_c = 1.025$ s and $\beta = 9.7 \cdot 10^{-3} \text{s}^{-1/2}$. In Case II, the modal activated diameter is $d_c = 9.141 \mu\text{m}$, giving $X_c = 0.2611$ s and $\beta = 1.4 \cdot 10^{-3} \text{s}^{-1/2}$. These modal values are obtained from the data of [18]. For Case III, though, since the system is subsaturated and haze particles are more numerous—see Table 1 of [18]—the term β is practically zero. The corresponding original Köhler and M-Köhler curves are shown in Fig. 6a) and b), as dashed and solid curves, respectively, and shown as functions of the diameter $d = 2\sqrt{2D\bar{X}}$. For Case III, because there is not sink term, only the original Köhler curve is shown.

Once the parameters for the relative disturbances, σ_1 , σ_2 and κ are chosen as listed in Table II, the corresponding Gibbs states ρ_λ given by Eq. (9) exhibit striking skills in reproducing the empirical DSDs in each of the three Pi-chamber experiments taken from [18]. The results are shown in the Figs. 6d), e) and f). The shapes of the Gibbs states are highly correlated to those of the transformed potentials shown in the insets of Fig. 6, obtained by the Lamperti transformation; see *Methods*. We observe in particular that the potential wells’ locations match the Gibbs states modes’ locations. Recall that the latter transformation allows for identifying the effective potential for the stochastic model (15) subject to size-dependent stochastic disturbances such as given by (14). With this effective potential, Eq. (15) can be interpreted as a Brownian particle evolving within that potential whose fluctuations are just driven by a white noise, independently of the size of the particle.

As sanity check, one observes that the experimental DSDs’ modes are well predicted by Eq. (11), as shown in Fig. 7 of *Noise-induced metastability*, especially in Cases I and II, where the classical Köhler theory is unable to predict an activated mode, since $\lambda > \lambda_K$. Noteworthy is the creation of a metastable haze-state in Case I resulting from the interaction between the noise term $\sigma(X) \dot{W}_t$ and the nonlinear drift terms $-f(X) - \beta X^{1/2}$ as revealed by the transformed potential shown in the inset of Figs. 6d); see *Noise-induced metastability* in *Methods*.

DISCUSSION

Köhler theory stands in the foundation of cloud physics. For a given dry aerosol size and composition, it predicts the particle’s state, haze, or activated droplet as a function of the particle size and the supersaturation. The Köhler curve (Fig. 1a), has two fixed-point regimes bounded by the curve’s mode. The curve left to the mode describes a stable fixed point, whereas any particle that resides on the curve right to the mode is on an unstable fixed point such that a perturbation to the right

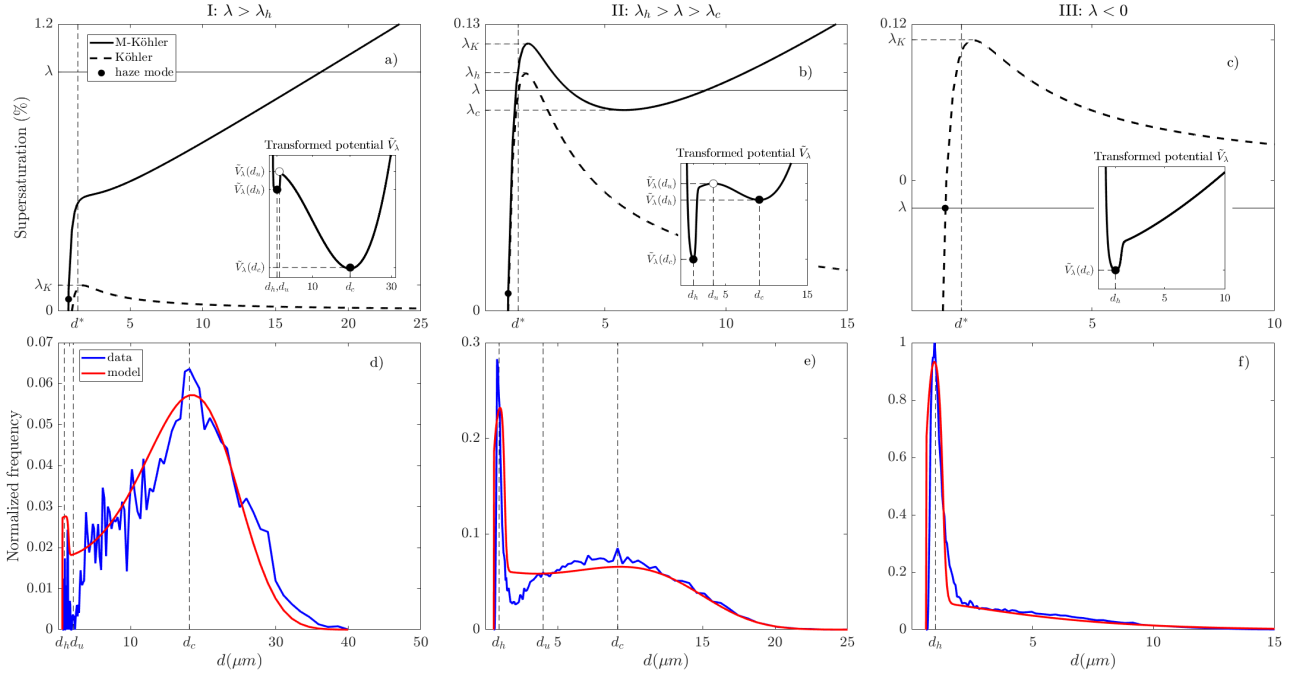


FIG. 6: **Panels a), b) and c):** Köhler and M-Köhler curves (dashed and solid curves, respectively) for each supersaturation value considered in *PI-Chamber Empirical Distribution vs Gibbs States* (Cases **I**, **II**, and **III**). The parameters of the Köhler curve are $A = 1.4 \cdot 10^{-3} \mu\text{m}$ and $B = 3.5 \cdot 10^{-4} \mu\text{m}^3$ and the other parameters of model Eq. (15) are given in Table II. The black dot denotes the location of the metastable state induced by the state-dependent noise; see *Noise-induced metastability in Methods*. **Panels d), e) and f):** Experimental DSDs from [18] vs Gibbs states from Eq. (9). Both the data histograms and Gibbs states are normalized according to their integral. The insets show the transformed potentials (due to Lamperti transformation) explaining the shapes of the Gibbs states; see *The Lamperti transformation in Methods*.

TABLE II: Supersaturation λ and parameter values of the sink term and state-dependent noise $\sigma(X)$ in Eq. (14).

	$\lambda \times 100$ (%)	β ($\text{s}^{-1/2}$)	σ_1 ($\text{s}^{1/2}$)	σ_2 ($\text{s}^{1/2}$)	d^* (μm)	$2\kappa D$
Case I	1	$9.6 \cdot 10^{-3}$	$3.75 \cdot 10^{-2}$	$6.25 \cdot 10^{-2}$	1.41	10
Case II	0.1	$1.4 \cdot 10^{-3}$	$7.5 \cdot 10^{-3}$	$1.5 \cdot 10^{-2}$	1.41	10
Case III	-1	0	$5 \cdot 10^{-3}$	$1.5 \cdot 10^{-2}$	1.41	10

(or upward) will shift the particle to a continuous growth by diffusion and a perturbation to the left (or downward) will send the particle to the haze state. Warm and small clouds that are driven by weak temperature or humidity perturbations [5, 21, 23] are superabundant and have an important radiative effect. However, due to their sizes, weak optical signature, and short lifetimes, these clouds are mostly overlooked, and their properties are poorly understood. Such clouds often exist near the transition between haze to cloud [36] a regime that can be studied in cloud chambers [18, 34].

Here, we address these clouds by extending Köhler theory to population of droplets embedded in turbulent environments. While activation is explained by Köhler's theory, the reverse process, i.e. deactivation, is dynamically different. It has been documented in previous works [9, 10] and in the present study that deactivation is intimately tied to the hysteresis phenomenon through which deactivation occurs at a smaller supersaturation compared to the critical Köhler value λ_K . The addition of a sink term in the condensational growth

equation—see Eq. (3)—yields hysteresis directly from an analytical perspective: in order to deactivate a family of monodisperse cloud droplets, the supersaturation needs to be brought strictly below the critical value λ_K predicted by Köhler, see Figs. 1b). The origin of this behavior is the presence of another saddle-node bifurcation that results from the bending of the M-Köhler curve introduced in *Multistable Köhler curves*. This bending translates further into the appearance of another stable equilibrium on the activated droplet spectrum as a balance between condensational instability and sink factors, like supersaturation consumption or particle removal. We refer to the section *Multistability in Methods* for conditions on the sink function g ensuring for such a bending to occur, and thus the creation of an extra saddle-node bifurcation in Eq. (3).

The introduction of Brownian noise in the condensational growth equation parameterizes the influence of supersaturation fluctuations and gives analytical formulas for computing DSDs, here identified as Gibbs states; see Eq. (9). Such probability distribution is a general formulation of DSDs found in

the literature [19, 22, 29], with the addition of size dependent fluctuations. The resulting DSDs are classified into three types according to the mean supersaturation parameter λ . The first corresponds to the case where supersaturation fluctuations do not have the strength to activate droplets for a prolonged period of time and, hence, the size distribution is unimodal around the haze state. In the second case, activation is allowed and if the threshold λ_h is surpassed, haze particles cease to be stable and a single DSD mode is observed peaking over the activated sizes. Consequently, even if Köhler's threshold supersaturation is not attained, there is a finite probability that particles activate and remain so stably. The associated timescales for activation is therefore related to the average time it takes to droplets to gain sufficient energy to surpass the potential barrier of activation— see Fig. 1c)—, and they are given precisely by Kramers' formula Eq. (12). In fact, when a cloud parcel is adiabatically cooled, supersaturation fluctuates around a slowly increasing mean. Neglecting noisy fluctuations would incur into an overestimation of the superstaruation threshold for activation, as shown in every panel of Fig. 5, where the interplay between noise and activation hysteresis is illustrated. It is realized that on an activation-deactivation cycle, on average, activation occurs at a much lower supersaturations compared to λ_h , and the larger the variance the lower such threshold is.

The confrontation of our population Köhler scheme within our Brownian modeling framework to steady-state cloud experiments conducted in the Pi-chamber has revealed a striking consistency. Particularly at capturing to a high degree of fidelity the complexity of the DSDs' shapes along with their bimodal features as reported in the experimental study of [18], for different saturation regimes. Under such a setting, it remains to investigate the slow adiabatic changes in mean supersaturation. Based on the analytical insights gained on the droplet activation-deactivation hysteresis (see Fig. 5), we foresee that the same hysteresis behavior should also be observed in the experimental framework of [18].

Weak clouds in nature are likely to be exposed to aerosols of several sizes and compositions. However, the weak supersaturation may act as a selective filter, making the largest haze bins the leading players, yielding conditions that are not so different from our theoretical setting. Moreover, the additional Brownian noise blurs the particles' homogeneity due to the monodisperse nature of the initial conditions. Nevertheless, cases with polydisperse particles of different chemical natures and, hence, different Köhler curves are planned to be investigated.

METHODS

Multistability. In order for model (3) to allow for multiple stable equilibria, it is enough if the the M-Köhler curve $f - g$ has at least a local minimum and a local maximum. This property is to guarantee that the zeros of $\lambda - (f - g)$ correspond to at least two stable equilibria and an unstable one, for a range of values of λ .

To simplify the presentation of the results stated in Proposition 1 below, we introduce the following parameters:

$$\tilde{A} = \frac{A}{(2D)^{1/2}}, \quad (17a)$$

$$\tilde{B} = \frac{B}{(2D)^{3/2}}. \quad (17b)$$

We then have the following sufficiency result for the existence of a local maximum and a local minimum:

Proposition 1. *Let f be the function given in Eq. (2) and let $g : \mathbb{R}^+ \rightarrow \mathbb{R}^-$ be a function of the form $g(X) = -\beta X^\alpha$, where $\beta > 0$ and $\alpha > 1$. If $\dot{g}(5\tilde{B}/\tilde{A}) > \dot{f}(5\tilde{B}/\tilde{A})$, the M-Köhler curve in Eq. (3) has at least a local maximum and a local minimum.*

Proof. We need to show that the function $\dot{f} - \dot{g}$ has two zeros, and thus it suffices to prove that $\dot{f} - \dot{g}$ has at least two changes of sign. This function reads, for $X > 0$, as:

$$\dot{f}(X) - \dot{g}(X) = -\frac{\tilde{A}}{2}X^{-3/2} + \frac{3\tilde{B}}{2}X^{-5/2} + \alpha\beta X^{\alpha-1}. \quad (18)$$

When $\alpha = 3/2$ as in Eq. (6), one recovers that finding the zeros of $\dot{f} - \dot{g}$ is equivalent to finding the roots of the polynomial equation (7).

First of all, \dot{f} has a single local and global minimum. Indeed, we see this by examining \ddot{f} :

$$\ddot{f}(X) = \frac{3}{4}\tilde{A}X^{-5/2} - \frac{15}{4}\tilde{B}X^{-7/2}, \quad (19)$$

which has a unique zero at $X = 5\tilde{B}/\tilde{A}$, and

$$\ddot{f}\left(\frac{5\tilde{B}}{\tilde{A}}\right) = -\frac{\tilde{A}}{5}\left(\frac{\tilde{A}}{5\tilde{B}}\right)^{\frac{3}{2}} < 0. \quad (20)$$

Furthermore, the two limits below hold:

$$\lim_{X \rightarrow 0^+} \dot{f}(X) = +\infty \quad (21a)$$

$$\lim_{X \rightarrow \infty} \dot{f}(X) = 0. \quad (21b)$$

These two limits together with Eq. (20) indicate that $X = 5\tilde{B}/\tilde{A}$ is a global minimum.

Because of the smoothness of f and g on \mathbb{R}^+ , the limit in Eq. (21a), and— by hypothesis— $\alpha > 1$, we have:

$$\lim_{X \rightarrow 0^+} \dot{f}(X) - \dot{g}(X) = +\infty, \quad (22)$$

there exists $X_1 > 0$ such that $\dot{f}(X_1) - \dot{g}(X_1) > 0$. Moreover, by hypothesis, $\dot{f}(5\tilde{B}/\tilde{A}) - \dot{g}(5\tilde{B}/\tilde{A}) < 0$, and that gives the first change of sign of the function $\dot{f} - \dot{g}$.

Lastly, by assumption we have that $\alpha > 1$, so the following limit holds

$$\lim_{X \rightarrow \infty} \dot{g}(X) = \lim_{X \rightarrow \infty} -\alpha\beta X^{\alpha-1} = -\infty. \quad (23)$$

Considering this limit and the one in Eq. (21b), there exists $X_2 > 5\tilde{B}/\tilde{A}$ such that $\dot{f}(X_2) - \dot{g}(X_2) > 0$. This gives the second change of sign.

Due to the continuity and smoothness of the functions f and g on \mathbb{R}^+ , the function $\dot{f} - \dot{g}$ must have at least two zeros. \square

The confining potential. In order for a gradient system to possess a Gibbs state, it is necessary that the associated potential is *confining* see e.g. [27, §4]. We provide here sufficient mathematical conditions by which a sink function g in Eq. (8) ensures the confining property. Generally, it amounts to imposing a sufficiently strong decay rate to the sink term.

The potential function V_λ is said to be confining if:

$$\lim_{X \rightarrow 0^+} V_\lambda(X) = \lim_{X \rightarrow \infty} V_\lambda(X) = \infty, \quad (24)$$

and if for any $\xi > 0$,

$$\int_0^\infty e^{-\xi V_\lambda(X)} dX < \infty. \quad (25)$$

Below, we provide a class of sink functions for which the associated M-Köhler curve has a confining potential.

Proposition 2. Let λ be in \mathbb{R} , f be as in Eq. (2) and let $g : \mathbb{R}^+ \rightarrow \mathbb{R}^-$ be defined as $g(X) = -\beta X^\alpha$, for $X, \alpha, \beta > 0$. Then, the potential V_λ associated with Eq. (8) is confining.

Proof. By the definition of f , g and the potential V_λ , we find that:

$$-V_\lambda(X) = \int^X (\lambda - f(X) + g(X)) dX \quad (26a)$$

$$= \lambda X - 2\tilde{A}X^{1/2} - 2\tilde{B}X^{-1/2} - \frac{\beta}{1+\alpha}X^{1+\alpha}, \quad (26b)$$

where the parameters \tilde{A} and \tilde{B} are defined in Eq. (17). Then,

$$\lim_{X \rightarrow 0^+} V_\lambda(X) = \lim_{X \rightarrow 0^+} 2\tilde{B}X^{-1/2} = \infty, \quad (27a)$$

$$\lim_{X \rightarrow \infty} V_\lambda(X) = \lim_{X \rightarrow \infty} \frac{\beta}{1+\alpha}X^{1+\alpha} = \infty. \quad (27b)$$

We are left with showing the integrability condition (25). The integral of the exponential of the potential satisfies, for any $\xi > 0$, the following inequalities:

$$\int_0^\infty e^{-\xi V_\lambda(X)} dX \quad (28a)$$

$$= \int_0^\infty e^{\xi(\lambda X - 2\tilde{A}X^{1/2} - 2\tilde{B}X^{-1/2} - \frac{\beta}{1+\alpha}X^{1+\alpha})} dX \quad (28b)$$

$$\leq \int_0^\infty e^{\xi(\lambda X - \frac{\beta}{1+\alpha}X^{1+\alpha})} dX \quad (28c)$$

$$= \int_0^\infty e^{-X(\frac{\xi\beta}{1+\alpha}X^\alpha - \xi\lambda)} dX \quad (28d)$$

$$\leq \int_0^{X_0} e^{-X(\frac{\xi\beta}{1+\alpha}X^\alpha - \xi\lambda)} dX + \int_{X_0}^\infty e^{-X} dX < \infty, \quad (28e)$$

for any $\xi > 0$ and where $X_0 = ((1 + \xi\lambda)(1 + \alpha)/\xi\beta)^{1/\alpha}$ is such that:

$$\frac{\xi\beta}{1+\alpha}X_0^\alpha - \xi\lambda = 1. \quad (29)$$

This proves the confining property. \square

Hysteresis path algorithm. To produce the hysteresis paths shown in Fig. 5, we solve Eq. (6) for slowly varying values of the supersaturation parameter λ and Brownian noise's parameter σ taken to be additive, i.e. $\sigma(X) = \sqrt{2\varepsilon}$. The slow drift of the supersaturation parameter is organized as follows. We start by dividing an interval $[\lambda_0, \lambda_{N+1}] \supset (\lambda_c, \lambda_h)$ uniformly into $N + 2$ grid points $\{\lambda_j\}_{j=0}^{N+1}$ such that $\lambda_j = \lambda_0 + j\delta\lambda$, with $\delta\lambda = (\lambda_h - \lambda_c)/(N - 1)$ and $\lambda_0 = \lambda_c - \delta\lambda/2$. Note that $\lambda_{N+1} > \lambda_h$ and $\lambda_N < \lambda_h$.

To form the lower branch of this hysteresis path, we start with $\lambda = \lambda_0$ and from the haze state $X_h(\lambda_0)$, and solve Eq. (6) using an Euler-Maruyama scheme [37, Chapter 9.1] for one timestep; $dt = 1$. Then λ is updated to $\lambda_0 + j\delta\lambda$ and Eq. (6) is iterated over another timestep by still using Euler-Maruyama. The process is repeated $N + 1$ times until $\lambda_{N+1} > \lambda_h$. The reverse trajectory is obtained by repeating the algorithm, although starting with $\lambda = \lambda_{N+1}$ at $X_c(\lambda_{N+1})$. More precisions are given in Algorithm 1 and hereafter.

The key parameter to produce panels a), b) and c) of Fig. 5 is λ . Note that according to the previous algorithm, $\lambda \approx \delta\lambda/\delta t$. Consequently, the larger N is, the smaller $\delta\lambda$, and vice versa.

The Lamperti transformation. For scalar stochastic differential model, it is possible to map a stochastic differential equation (SDE) driven by state-dependent noise onto an SDE driven by an additive noise. We recall this basic idea. Consider the following scalar SDE

$$\dot{X} = -V(X) + \sigma(X)\dot{W}_t, \quad (30)$$

Algorithm 1 Hysteresis path computation

- 1: δt and N is prescribed by the user
 - 2: $\delta\lambda = (\lambda_h - \lambda_c)/(N - 1)$
 - 3: $\lambda_{vals}^+ = \{\lambda_0 + j\delta\lambda\}_{j=0}^{N+1}$, with $\lambda_0 = \lambda_c - \delta\lambda/2$
 - 4: $\lambda_{vals}^- = \{\lambda_{N+1} - j\delta\lambda\}_{j=0}^{N+1}$
 - 5: Form the set $\lambda_{vals} = \{\lambda_{vals}^+, \lambda_{vals}^-\}$
 - 6: Let X be a $2(N + 2)$ -dimensional vector approximating the hysteresis path
 - 7: We choose the initial datum to be $X_h(\lambda_0)$, i.e. $X(1) = X_h(\lambda_0)$
 - 8: **for** $j = 0 : 2N + 3$ **do**
 - 9: $\mu = \lambda_{vals}(j + 1)$
 - 10: % Euler-Maruyama scheme to integrate Eq. (3)
 - 11: $X(j + 1) = X(j) - \delta t V_\mu(X(j)) + \sqrt{2\varepsilon\delta t}\zeta_j$, where ζ_ℓ are independent normally distributed random variables with mean zero and variance unity
 - 12: **end for**
-

with V and σ smooth functions, such that $\sigma > 0$. Consider the change of variables, $h(X) = \int^X \frac{1}{\sigma(X)} dX$, then by application of Itô's formula, the original equation (30) is transformed into

$$\dot{Y} = -\hat{V}(Y) + \dot{W}_t, \quad (31)$$

with

$$\hat{V}(Y) = \frac{V(h^{-1}(Y))}{\sigma(h^{-1}(Y))} - \frac{1}{2}\sigma'(h^{-1}(Y)). \quad (32)$$

This is called the Lamperti transformation [27, §3.6].

The Lamperti transformation allows for identifying the *effective potential*, \hat{V} , for the stochastic model (30) subject to state-dependent stochastic disturbances given by $\sigma(X)\dot{W}_t$. With this effective potential, Eq. (30) can be interpreted as a Brownian particle evolving within that potential whose fluctuations are just driven by a white noise, independently of the state X . In particular even if the original potential V does not exhibit a well over a certain range of X -values, the transformed potential can exhibit such local minimum. We talk then of noise-induced metastability in case of creation of an extra metastable state resulting from the interaction of the drift term with the diffusion term $\sigma(X)\dot{W}_t$.

Noise-induced metastability. By applying (32) to our stochastic droplet model (15) in Pi-chamber, we obtain:

$$\hat{V}'_\lambda(Y) = -\frac{V'_\lambda(X)}{\sigma(X)} - \frac{1}{2}\sigma'(X), \text{ with } Y = \int^X \sigma^{-1}(X) dX, \quad (33)$$

in which $V'_\lambda(X) = -\lambda + f(X) + \beta X^{-1/2}$.

Note that the appearance of equilibria non-trivially depends on both the potential V_λ and the noise function σ . Indeed, as a consequence of Eq. (33), the metastable states are explicitly given by solving $\hat{V}'_\lambda(Y) = 0$, namely by solving:

$$-V'_\lambda(X) = \frac{1}{2}\sigma'(X)\sigma(X), \quad (34)$$

recovering this way Eq. (11). Thus, if one wishes to match the locations of these metastable states with let us say the modes of an empirical distribution (as in *PI-Chamber Empirical Distributions vs Gibbs States*), one needs to solve Eq. (34). As a consequence, this equation imposes constraints on the choice of the parameters involved in σ and V_λ .

More precisely, we have that (34) rewrites as

$$\lambda - \tilde{A}X^{-1/2} + \tilde{B}X^{-3/2} - \beta X^{1/2} = \frac{1}{2}\sigma'(X)\sigma(X), \quad (35)$$

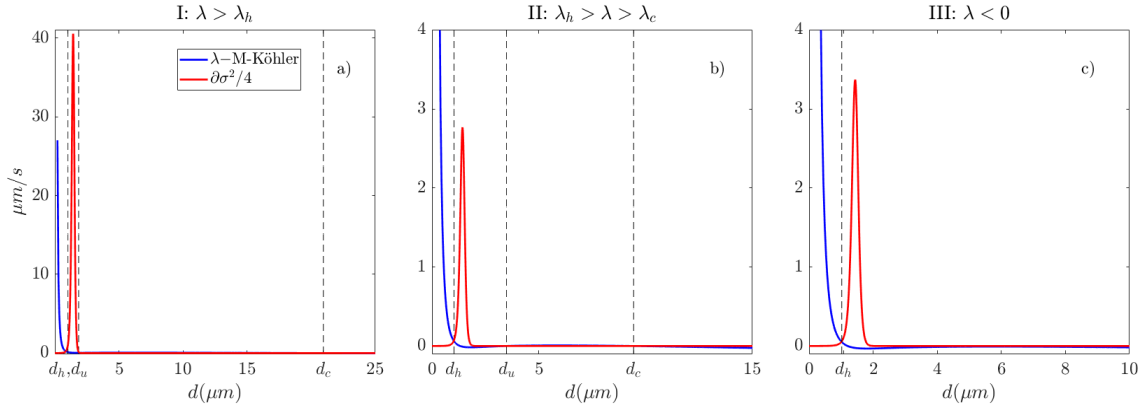


FIG. 7: **Noise-induced metastable states.** Panels a), b) and c), correspond to the three different supersaturation configurations as indicated in the titles and corresponding to those of Fig. 6. The blue curves show the growth rate function $-V'_\lambda$ in Eq. (8), such as associated with the M-Köhler curve $f(X) + \beta X^{1/2}$. The red curves show the derivative of the noise covariance after division by a factor four corresponding to the RHS of Eq. (34). The vertical dashed lines indicate the location of the solutions to Eq. (34) which also correspond to the haze, unstable and activated metastable states, denoted by d_h , d_u and d_c , respectively.

where \tilde{A} and \tilde{B} are defined in Eq. (17). By observing that $\sigma(X) = \sigma_1 + \frac{\sigma_2 - \sigma_1}{2} (1 + \tanh(\kappa(X - X^*))) \rightarrow 0$ as $X \rightarrow \infty$, one can get then, when $\kappa \gg 1$ and X is sufficiently larger than X^* , good approximations of the solutions X to Eq. (35) by solving:

$$\lambda X^{3/2} - \tilde{A}X + \tilde{B} - \beta X^2 = 0, \quad (36)$$

We adopt this strategy for Cases I and II of PI-Chamber Empirical Distribution vs Gibbs States.

The sink parameter β has a direct influence on the location of the metastable states and vice versa. One can invert equations (36) to find the value of β in terms of the activated mode X_c :

$$\beta = \frac{1}{X_c^2} \left(\lambda X_c^{3/2} - \tilde{A}X_c + \tilde{B} \right), \quad (37)$$

leading thus to Eq. (16).

The blue and red curves in Fig. 7 correspond to the left-hand-side (LHS) and right-hand-side (RHS) of Eq. (34), respectively, for the three case studies of *PI-Chamber Empirical Distributions vs Gibbs States*. The intersection of these two curves determines the location of the metastable states indicated by the dashed vertical lines for Cases I, II and III with the parameter configuration shown in Table II.

Acknowledgements This work has been partially supported by the European Research Council (ERC) under the European Union's Horizon 2020 research and innovation program (grant agreement no. 810370). MSG is grateful to the Feinberg Graduate School for their support through the Dean of Faculty Fellowship.

Author contributions: MDC conceived the presented idea. MSG led the analyses and MDC supported. MSG, MDC, OA, and IK discussed the results and wrote the manuscript. All co-authors provided critical feedback and helped shape the research, analysis and manuscript.

Competing interests: The authors declare no competing interests.

Data availability: All experimental data used in this study are based on the article of [18] and are publicly available at: <https://digitalcommons.mtu.edu/data-files/3/>. The numerical data obtained for this article are available upon request to the authors.

-
- [1] L. Bengtsson, *Environmental Research Letters* **5**, 025202 (2010).
 - [2] M. D. Zelinka, T. A. Myers, D. T. McCoy, S. Po-Chedley, P. M. Caldwell, P. Ceppi, S. A. Klein, and K. E. Taylor, *Geophysical Research Letters* **47**, e2019GL085782 (2020).
 - [3] I. Koren, L. A. Remer, Y. J. Kaufman, Y. Rudich, and J. V. Martins, *Geophysical research letters* **34** (2007).
 - [4] T. Várnai and A. Marshak, *Geophysical Research Letters* **36** (2009).
 - [5] E. Eytan, I. Koren, O. Altartatz, A. Kostinsky, and A. Ronen, *Nature Geoscience* **13**, 669 (2020).
 - [6] A. P. Khain and M. Pinsky, *Physical Processes in Clouds and Cloud Modeling* (Cambridge University Press, 2018).
 - [7] R. R. Rogers and M. Yau, *A Short Course in Cloud Physics*, 3rd ed. (Pergamon Press Oxford, New York, 1989) pp. xiv, 293 p.
 - [8] H. Köhler, *Trans. Faraday Soc.* **32**, 1152 (1936).
 - [9] A. V. Korolev and I. P. Mazin, *J. Atmos. Sci.* **60**, 2957 (2003).
 - [10] S. Arabas and S. Shima, *Nonlinear Processes in Geophysics* **24**, 535 (2017).
 - [11] Y. A. Kuznetsov, *Elements of Applied Bifurcation Theory* (Springer, 2004).
 - [12] R. Shaw, *Annual Review of Fluid Mechanics* **35**, 183 (2003).
 - [13] G. Sardina, F. Picano, L. Brandt, and R. Caballero, *Physical review letters* **115**, 184501 (2015).
 - [14] W. W. Grabowski and G. C. Abade, *Journal of the Atmospheric Sciences* **74**, 1485 (2017).
 - [15] G. C. Abade, W. W. Grabowski, and H. Pawlowska, *Journal of the Atmospheric Sciences* **75**, 3365 (2018).
 - [16] P. R. Field, A. A. Hill, K. Furtado, and A. Korolev, *Quarterly Journal of the Royal Meteorological Society* **140**, 870 (2014).
 - [17] K. Furtado, P. R. Field, I. A. Boutle, C. J. Morcrette, and J. M. Wilkinson, *Journal of the Atmospheric Sciences* **73**, 279 (2016).
 - [18] P. Prabhakaran, A. S. M. Shawon, G. Kinney, S. Thomas, W. Cantrell, and R. A. Shaw, *Proceedings of the National*

- Academy of Sciences **117**, 16831 (2020).
- [19] S. K. Krueger, *Atmospheric Chemistry and Physics* **20**, 7895 (2020).
 - [20] E. Hirsch, I. Koren, Z. Levin, O. Altaratz, and E. Agassi, *Atmospheric Chemistry and Physics* **14**, 9001 (2014).
 - [21] O. Altaratz, I. Koren, E. Agassi, E. Hirsch, Y. Levi, and N. Stav, *Geophysical research letters* **48**, e2021GL096242 (2021).
 - [22] K. K. Chandrakar, I. Saito, F. Yang, W. Cantrell, T. Gotoh, and R. A. Shaw, *Quarterly Journal of the Royal Meteorological Society* **146**, 483 (2020), <https://rmets.onlinelibrary.wiley.com/doi/pdf/10.1002/qj.3692>.
 - [23] E. Hirsch, I. Koren, O. Altaratz, Z. Levin, and E. Agassi, *Environmental Research Letters* **12**, 024020 (2017).
 - [24] J. M. Wallace and P. V. Hobbs, *Atmospheric Science, an Introductory Survey* (Elsevier, 2006).
 - [25] N. Berglund, (2011), [10.48550/ARXIV.1106.5799](https://arxiv.org/abs/10.48550/ARXIV.1106.5799).
 - [26] C. Siewert, J. Bec, and G. Krstulovic, *Journal of Fluid Mechanics* **810**, 254 (2017).
 - [27] G. A. Pavliotis, *Stochastic Processes*, Vol. 60 (Springer, New York, 2014).
 - [28] H. Risken, *The Fokker-Planck Equation*, 2nd ed. (Springer, 1989).
 - [29] R. McGraw and Y. Liu, *Geophysical Research Letters* **33** (2006), [10.1029/2005GL023545](https://doi.org/10.1029/2005GL023545).
 - [30] H. Kramers, *Physica* **7**, 284 (1940).
 - [31] B. J. Matkowsky and Z. Schuss, *SIAM Journal on Applied Mathematics* **40**, 242 (1981).
 - [32] N. Berglund and B. Gentz, *Nonlinearity* **15**, 605 (2002).
 - [33] I. Koren, L. Oreopoulos, G. Feingold, L. Remer, and O. Altaratz, *Atmospheric Chemistry and Physics* **8**, 3855 (2008).
 - [34] K. K. Chandrakar, W. Cantrell, K. Chang, D. Ciochetto, D. Niedermeier, M. Ovchinnikov, R. A. Shaw, and F. Yang, *Proceedings of the National Academy of Sciences* **113**, 14243 (2016).
 - [35] P. Squires, *Tellus* **8**, 443 (1956).
 - [36] I. Koren, G. Feingold, H. Jiang, and O. Altaratz, *Geophysical Research Letters* **36** (2009).
 - [37] P. E. Kloeden and E. Platen, *Numerical Solution of Stochastic Differential Equations*, Vol. 23 (Springer Berlin Heidelberg).